Developmental Cell

Article

Cell
P R E S S

Organism-Scale Modeling of Early *Drosophila* Patterning via Bone Morphogenetic Proteins

David M. Umulis,[1] Osamu Shimmi,[2] Michael B. O'Connor,[3,*] and Hans G. Othmer[4,*]

[1]Agricultural and Biological Engineering, Weldon School of Biomedical Engineering, and Bindley Bioscience Center, 225 South University Street, Purdue University, West Lafayette, IN 47907, USA
[2]Institute of Biotechnology, University of Helsinki, 00014 Helsinki, Finland
[3]Howard Hughes Medical Institute, and Department of Genetics, Cell Biology, and Development
[4]School of Mathematics and Digital Technology Center
University of Minnesota, Minneapolis, MN 55455, USA
*Correspondence: moconnor@umn.edu (M.B.O.), othmer@math.umn.edu (H.G.O.)
DOI 10.1016/j.devcel.2010.01.006

SUMMARY

Advances in image acquisition and informatics technology have led to organism-scale spatiotemporal atlases of gene expression and protein distributions. To maximize the utility of this information for the study of developmental processes, a new generation of mathematical models is needed for discovery and hypothesis testing. Here, we develop a data-driven, geometrically accurate model of early *Drosophila* embryonic bone morphogenetic protein (BMP)-mediated patterning. We tested nine different mechanisms for signal transduction with feedback, eight combinations of geometry and gene expression prepatterns, and two scale-invariance mechanisms for their ability to reproduce proper BMP signaling output in wild-type and mutant embryos. We found that a model based on positive feedback of a secreted BMP-binding protein, coupled with the experimentally measured embryo geometry, provides the best agreement with population mean image data. Our results demonstrate that using bio-images to build and optimize a three-dimensional model provides significant insights into mechanisms that guide tissue patterning.

INTRODUCTION

In many systems, spatially patterned cellular differentiation is regulated by signaling molecules called morphogens, which initiate spatiotemporal patterns of gene expression in a concentration-dependant manner (Turing, 1952; Wolpert, 1969; Driever and Nusslein-Volhard, 1988; Reeves et al., 2006). In early *Drosophila* embryos, a morphogen composed of a heterodimer of Decapentaplegic (Dpp) and Screw (Scw), two members of the bone morphogenetic protein (BMP) family (Figures 1A and 1B), directs patterning of the dorsal ectoderm (Shimmi et al., 2005; O'Connor et al., 2006). Unlike classical morphogen systems that rely on the slow spreading of a molecule from

a localized source to establish a gradient, BMPs in the early *Drosophila* embryo are secreted from a broad region making up the dorsal-most 40% of the embryo circumference. Subsequently, they are dynamically concentrated into a narrow region centered about the dorsal midline that makes up only 10% of the embryo circumference (Figures 1A and 1B) (Sutherland et al., 2003; Wang and Ferguson, 2005; O'Connor et al., 2006).

A number of extracellular regulators contribute to the dynamics and localization of BMP signaling (Figures 1B and 1C). Laterally secreted Short gastrulation (Sog) and dorsally secreted Twisted gastrulation (Tsg) diffuse from their regions of expression and form a heterodimer inhibitor (Sog/Tsg) that binds to Dpp-Scw, preventing it from binding to receptors. The cell matrix may mediate the formation of this complex, as it has recently been shown that collagen can bind both BMPs and Sog, thereby facilitating their association (Figure 1D) (Wang et al., 2008). The extracellular binding reactions lead to a gradient of inhibitor-bound Dpp-Scw that is high laterally and low at the dorsal midline, and an opposing gradient of free Dpp-Scw that is high at the dorsal midline. The dorsally secreted metalloprotease Tolloid (Tld) processes Sog only when Sog is bound to BMP ligands, and the degradation of Sog by Tld further enhances both the gradient of inhibitor-bound Dpp-Scw and of free Dpp-Scw. Thus, extracellular Dpp-Scw is redistributed by a combination of binding to inhibitor, processing of this complex, and diffusion.

Simultaneously, receptors and other surface-localized binding proteins compete with Sog to bind the available Dpp-Scw. Dpp-Scw activates signaling by binding to and recruiting the *Drosophila* type I receptors, Thickveins (Tkv) and Saxophone (Sax), into a high-order complex containing two subunits of the type II receptor Punt (Shimmi et al., 2005). The receptor complex phosphorylates Mad (pMad), a member of the Smad family of signal transducers, and phosphorlyated Mad binds to the co-Smad Medea, forming a complex that then accumulates in the nucleus, where it regulates gene expression in a concentration-dependent manner (Schmierer et al., 2008).

Although complex formation and transport favor a net movement of ligand toward the dorsal midline of the embryo, positive feedback in response to pMad signaling is needed to further concentrate the surface-localized Dpp-Scw at the dorsal midline (Wang and Ferguson, 2005). A loss of extracellular BMP
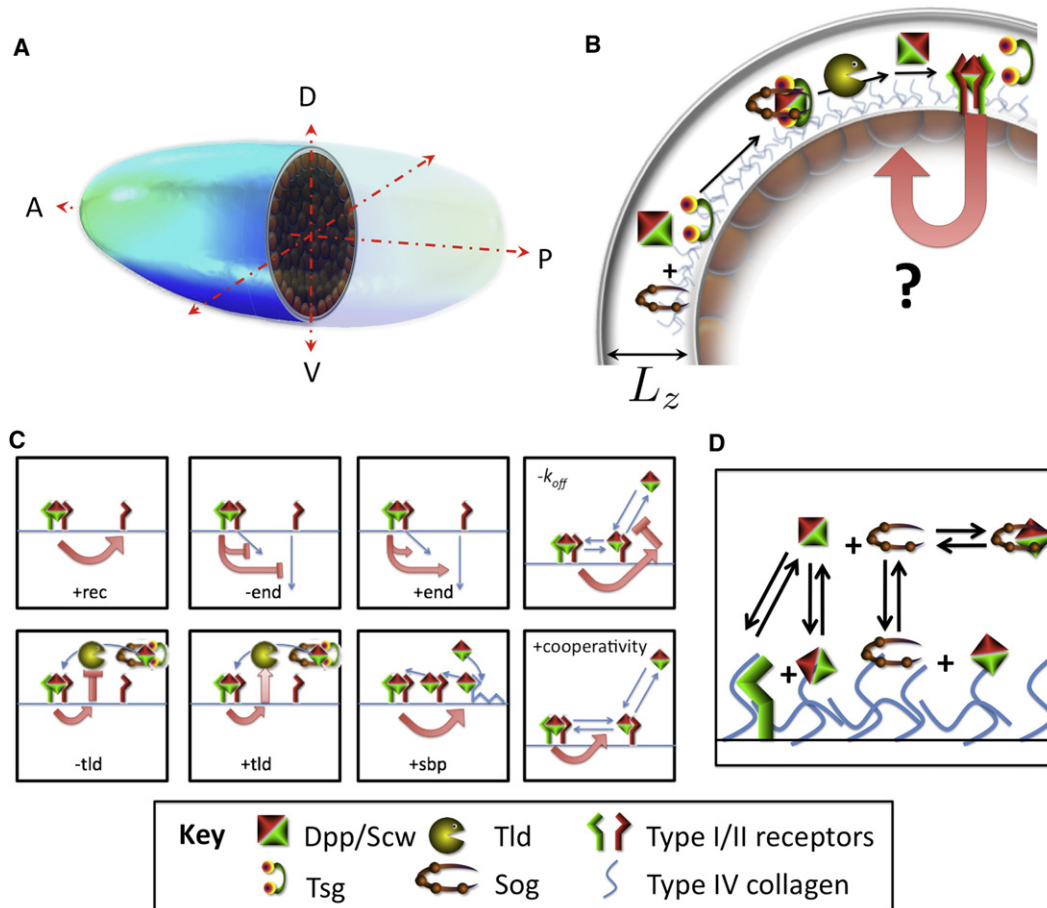
Figure 1. Introduction and Background

(A) Axis and geometry of a *Drosophila* blastoderm embryo.

(B) Schematic of the BMP DV patterning network (cross-section view; legend at the bottom of the figure). Note the "?" on the diagram for the positive feedback, which is still unknown.

(C) Alternative positive-feedback mechanisms for signal-induced regulation of extracellular BMPs. (+rec), positive feedback of receptor levels; (+/−end), positive and negative regulation of endocytosis; (-k_{off}), feedback inhibition of ligand release from receptor; (+/−tld), positive and negative regulation of Tld processing; (+cooperativity), positive regulation of type I/II/Dpp-Scw complex formation.

(D) Schematic of ligand-inhibitor complex formation in solution and after attached to collagen.

regulators or positive feedback impedes the attenuation of pMad laterally as well as the accumulation of pMad signaling at the dorsal midline. Although feedback, extracellular transport, and signal transduction each provide a specific mode of Dpp-Scw signal regulation, it is the dynamic interaction of these regulatory mechanisms that patterns the dorsal surface of *Drosophila* embryos. Not only does the mechanism work under optimal laboratory conditions, but dorsal surface patterning appears to be remarkably resilient to nonideal conditions such as temperature fluctuations, reductions in the level of regulatory factors such as Tsg, ectopic gene expression, and other perturbations (Eldar et al., 2002; Umulis et al., 2006). These issues illustrate the complexity of the problem and suggest that we can no longer rely solely on genetic and biochemical data to fully explain this rather simple patterning problem.

To address a number of unanswered questions about Dpp-Scw-mediated patterning and to take full advantage of the available data on *Drosophila* development, we developed

a methodology that seamlessly integrates biological information in the form of prepatterns, geometry, mechanisms, and training data into an organism-scale model of the blastoderm embryo that is based on a reaction-diffusion description of patterning. The mathematical model is simulated by using the widely available computational frameworks Comsol and Matlab (Figure 2; see Figure S1 available online), which makes extensive use of the model and methodology feasible.

We developed an image analysis protocol to obtain model training and initial condition data and to calculate population statistics for patterns of pMad signaling in *wild-type* (*wt*) and mutant *D. melanogaster*. We discovered that both the mean and variability of pMad signaling along the dorsal-ventral (DV) axis depends on anterior-posterior (AP) position and the specific choice of threshold. Using mutations previously considered robust, we were able to detect differences between mutant and wild-type pMad signaling patterns, which provided an information-rich data set for model training and for testing the
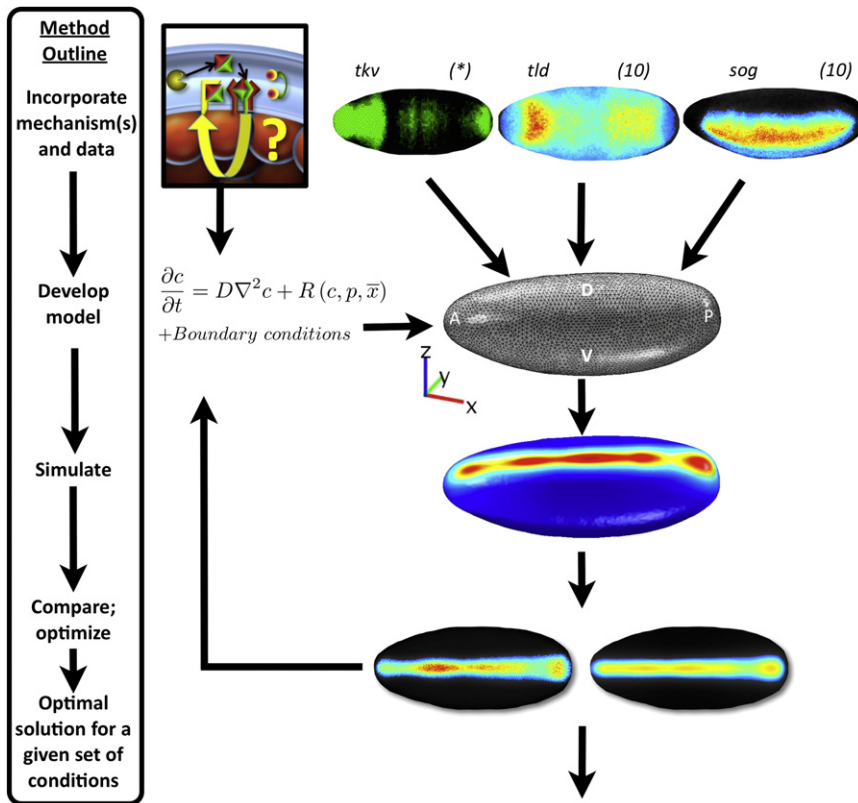
Developmental Cell

Figure 2. Workflow for the Development of a Data-Driven, Organism-Scale Model

Mechanism(s), prepatterns, and geometry are implemented into a 3D geometric representation of the *Drosophila* blastoderm embryo. Each model simulation gives the distribution of all secreted proteins and complexes along all axes of the embryo. The model's results are compared against the population mean distributions for pMad signaling in *wt* and eight additional mutants used for the model training. Each mechanism is optimized by comparing the predictions against image data, and alternative mechanisms can then be ranked based on their distance between the best fit and the actual image data.

contributions of diverse positive-feedback mechanisms and of proteins that concentrate BMPs at the cell surface. Unexpectedly, we found that geometry also has a large impact on the predicted patterns of BMP-bound receptors, whereas the prepatterned expression of receptors and other modulators of signaling did not greatly affect model-data correspondence. We found that if the embryo geometry is perturbed slightly in the model, then including the prepattern information greatly enhanced the model's ability to fit the observed pMad patterns, which suggests that the prepatterns may mitigate the effects of slightly misshapen embryos. We further identified conditions in the model that improve the scale invariance of patterning and tested the model predictions by staining for pMad in different species of *Drosophila*. These studies demonstrate that building a model based on image data and training the three-dimensional (3D) model against multidimensional expression data provide insights into the properties of several important developmental principles, including positive feedback, biological robustness, and scale invariance.

RESULTS AND DISCUSSION

Reproducibility of pMad Signaling in Late Cycle 14 Embryos

To begin our study, we first developed an image acquisition, normalization, and analysis strategy to obtain training and prepattern data for the model. To minimize errors in mounting and to normalize embryo geometries within a sample, individual embryo images were numerically rotated and reprojected into

an orientation with the dorsal side up (Figures S2 and S3). To normalize intensity measurements, we extended the method previously used for analyzing Bicoid intensity distributions (Gregor et al., 2007b) (Figures S2 and S3). pMad signaling distributions between embryos within a population are highly reproducible, as shown in Figure 3A. After analysis within a population, we compared pMad patterns between *D. melanogaster wt* and other perturbed populations, including embryos with homozygous and heterozygous mutations in BMP signaling components, hypomorphic alleles of pathway members, ectopic expression of pathway genes, and embryos from different species of *Drosophila* (mean distributions for *wt* and three heterozygous mutant populations are shown in Figure 3B). First, for *wt* embryos, we measured the width and variability of pMad level sets for different choices of the concentration thresholds (T). Embryo-to-embryo variability in the mean pMad width (μ) (measured in microns [μm]) for a given T value is quantified by the coefficient of variation (CV = σ/μ), a dimensionless quantity that relates the standard deviation σ to the mean along the entire AP axis (Figure 3C; Figures S4–S6). From T $\approx$ 0.15 to T $\approx$ 0.4, the CV for width is less than $\sim$0.2, which corresponds to $\sim\pm$2 nuclei in the cross-section. The variability of the CV along the AP axis is minimized at T $\approx$ 0.2–0.25 (Figure 3C) and increases as the threshold is increased. Thus, the embryo-to-embryo variability is minimized at relatively low thresholds of $\approx$20% of the maximum observed pMad signaling amplitude, which defines the range of thresholds in which we expect to have the greatest ability to detect differences between populations of *wt* and mutant embryos.

Variability of pMad Distributions

Whether or not the pMad distributions in dorsal blastoderm cells are insensitive to changes in gene copy number is unresolved, as different groups have arrived at different conclusions (Mizutani et al., 2005; Wang and Ferguson, 2005; Eldar et al., 2002; Shimmi et al., 2005; Umulis et al., 2008). To quantify the "robustness" or insensitivity of the patterns, we measured the difference in width of normalized pMad between *wt* and perturbed cases at
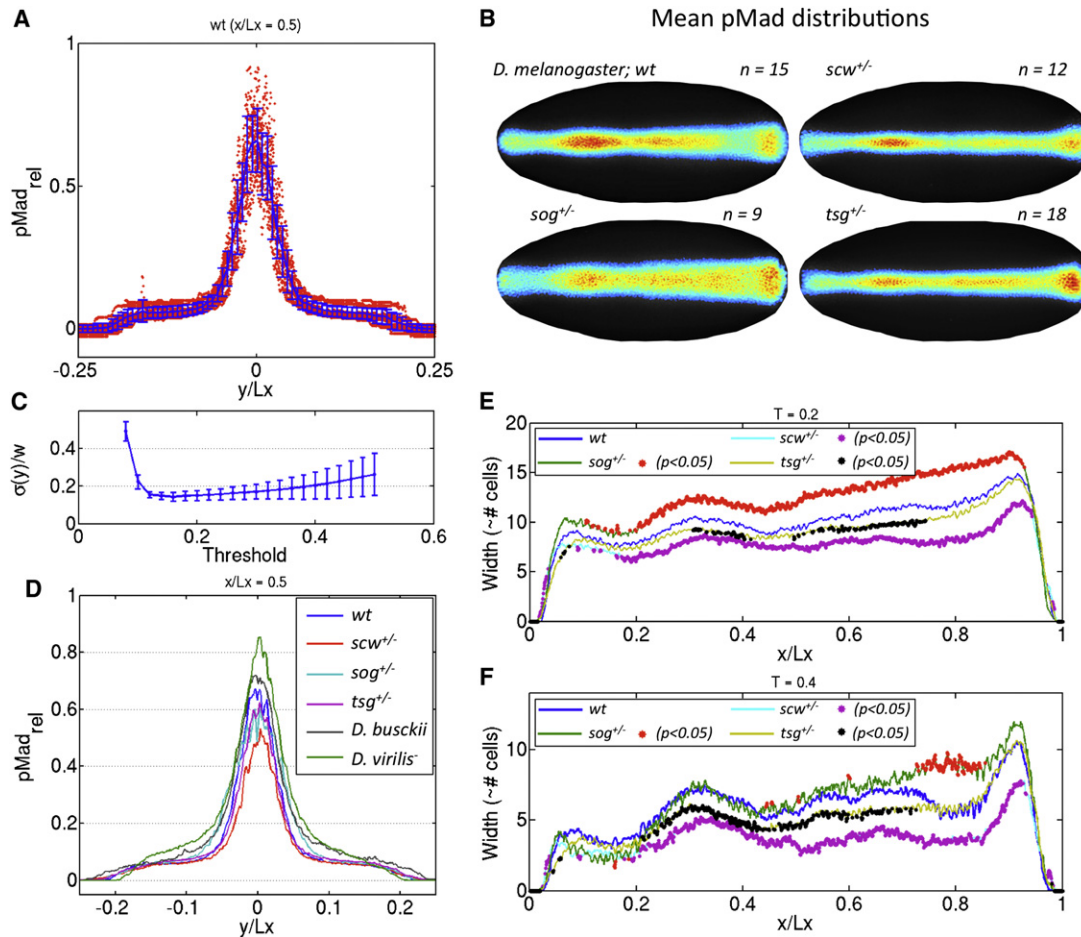
Figure 3. pMad Variability and Population Statistics

(A) Normalized *wt* pMad level versus position y/L_x at the cross-section $x/L_x = 0.5$. L_x is the mean length of the AP axis. Red dots are the normalized concentration, the solid blue line is the mean pMad in the cross-section, and the error bars correspond to $\pm\sigma$.

(B) Composite pMad distribution for (beginning at top left) *D. melanogaster wt* (n = 15), $scw^{+/-}$ (n = 12), $sog^{+/-}$ (n = 9), and $tsg^{+/-}$ (n = 18).

(C) Mean coefficient of variation for pMad width averaged along the AP axis for *wt* as a function of threshold (CV = σ/μ: standard deviation/width). Error bars (standard deviation of CV) provide a measure of CV variability along the AP axis.

(D) Mean pMad distribution along a cross-section at $x/L_x = 0.5$.

(E and F) Mean width of pMad varies along the AP axis. Thin lines represent the average width for the respective embryos (see legend in the upper-left portion of the figure). Colored data points are superimposed over the lines for the mean width in regions at which the null hypothesis (mean widths between the mutant and *wt* are equal) is rejected with $\alpha = 0.05$. Threshold values: (E) T = 0.2 and (F) T = 0.4.

threshold positions up to 40% of the maximum normalized *wt* level. Prior analysis that compared the mean width of pMad signal intensity at different cross-sections chosen along the AP axes did not take into account embryo-to-embryo variability of the population (Mizutani et al., 2005; Wang and Ferguson, 2005; Eldar et al., 2002; Shimmi et al., 2005). Furthermore, earlier studies did not consider the potential differences in pattern variability between different positions along the AP axis. At 50% embryo length ($x/L_x = 0.5$), the relative levels of mean pMad signaling vary greatly in amplitude near the DV midline ($y/L_x = 0$), but it is not clear if there are measurable differences between the width of the pMad profile for different level sets between T = 0.2 and 0.4 (Figure 3D). Furthermore, Figure 3C shows that the variability of the width in pMad varies along the AP axis and depends on the specific T-level used for the comparison of the patterns.

Given that earlier approaches to investigating the question of pattern robustness were based on one or two cross-sections at a single threshold level where there can be substantial variability, it is easy to see that different conclusions could be drawn from equivalent data sets, thus leading to debate in regards to the robustness of patterning.

Before an appropriate measure of robustness for pMad signaling patterns between different genotypes can be developed, one must first consider the natural variability that exists within each population. As a minimal criterion, we propose that if one cannot reject the null hypothesis in a Student's t test for a comparison of widths at a threshold level between two sample populations, then the patterning mechanism is by default robust. However, measuring a difference in the width of pMad does not preclude robustness, because a definition of robustness must

Developmental Cell

follow, not precede, the measurement of a statistically significant difference between populations.

To compare pMad distributions between different populations of embryos that each have a deficiency in the level of at least one BMP regulator (Figure 3D), we used the Student's t test of significance on the width of pMad level sets for specific threshold concentrations of 20% and 40% of the maximum scaled concentration (Figures 3D–3F; Figure S4). With an α value of 0.05 as the significance criterion, we found large segments along the AP axis where the null hypothesis (equal means) was rejected. This suggests that there are statistically significant, measurable differences in the width of pMad staining for specific threshold levels, particularly for the *sog* and *scw* heterozygous mutants. Surprisingly, the ability to reject the null hypothesis depends strongly on the specific threshold of pMad. For low threshold values (T = 0.2), the width of pMad in $sog^{+/-}$ embryos is ≈2–4 nuclei (cells) wider than *wt*, but for higher threshold values (T = 0.4), the width of pMad is virtually indistinguishable from *wt* for the majority of the AP length (compare Figure 3E and Figure 3F, $sog^{+/-}$ line). In *D. melanogaster*, heterozygous mutants are viable under standard laboratory nutrient and temperature conditions of 18°C–25°C, suggesting that the measurable changes in pMad signaling do not significantly disrupt development. In the context of dorsal surface patterning by BMPs, the image analysis data demonstrate that there are measurable differences between the pMad distributions of *wt* and heterozygous mutant embryos, which provide related, but unique, data sets that can be used for model testing and optimization.

After the normalization of pMad between populations of *wt* and mutant embryos, we extended the methodology to quantify distributions of gene expression of upstream components with the principal goal of incorporating quantitative prepattern information directly into a mathematical model of BMP regulation. Previous work has demonstrated approximate boundaries of gene expression for *dpp*, *tsg*, *sog*, *tld*, and *tkv* based on alkaline phosphatase staining, but a recent report on the *bcd* mRNA distribution demonstrated that detecting mRNA expression by alkaline phosphatase is much less quantitative than fluorescent in situ hybridization (FISH) (Spirov et al., 2009). Quantitative gene expression patterns for *tkv* (Fowlkes et al., 2008), *sog*, and *tld* were obtained, but we were unable to quantify the expression of *tsg* and *dpp* by FISH, and boundaries were approximated from alkaline phospatase-stained images (Figure 4A).

Comparison of BMP-Mediated Feedback Mechanisms

There are three general issues that can be addressed by using a 3D model that cannot be addressed by 1D models. The molecular mechanisms of BMP patterning have been inferred, in part, from the pMad distribution in embryos in which DV patterning genes are ectopically expressed along the AP axis, either by using the Gal4-UAS system or by injection of mRNA. Although pMad dynamics suggest a role for positive feedback, additional evidence for positive feedback is based on nonuniform AP distributions of pMad, pMad signaling losses, and the distribution of surface-bound Dpp in embryos injected with activated *tkv* mRNA on the dorsal surface (Wang and Ferguson, 2005). Thus, any model that postulates the molecular nature of the

positive feedback must be able to reproduce the observed AP pMad signaling profile and the pattern of surface-bound Dpp (Wang and Ferguson, 2005). Second, earlier models were developed and tested against 1D data, which greatly reduced the information density used for model optimization and hypothesis testing. Building a mathematical model based on quantitative biological images and training the model against multidimensional image data introduces additional constraints without increasing the number of unknowns. This should increase our ability to compare alternative, plausible mechanisms that could provide new insight into the regulation of BMP signaling. Finally, by using a 3D model, one can determine the sensitivity of pMad signaling and/or other patterns of activity to perturbations in geometry, size, and gene expression prepatterns.

To measure the relative contributions of (1) embryo geometry, (2) upstream gene expression, and (3) the specific choice of positive-feedback mechanism, we developed several different versions of the embryonic patterning model. To measure the role of geometry in patterning, we constructed two different model geometries of the embryo: (1) an embryo in the shape of a symmetrical prolate ellipsoid; and (2) a reconstruction of an experimentally determined nonsymmetric embryo derived from the VirtualEmbryo (Fowlkes et al., 2008). To avoid excessive computational time, we separated the analysis of positive feedback from the analysis of gene expression and embryo shape. First, we investigated alternative positive-feedback mechanisms by using only the realistic embryo shape with constant *tkv* and *tld*, and after a positive-feedback mechanism was selected, we used it for all further studies to determine the dependence of the model results on embryo shape and upstream gene expression patterns. For each different geometry and gene expression scenario, we allowed the parameters for the "winning" positive-feedback mechanism to be reoptimized to remove any bias toward a specific geometry and/or gene expression pattern.

To investigate the role of feedback, we developed nine versions of the model that differed in the specific molecular mechanism of feedback (Figure 1C). (Equations and parameters are provided in the Supplemental Experimental Procedures.) The models for the test were selected based upon the idea of "mechanism" conservation. Whereas the core signal transduction pathway for BMP signaling is widely conserved, the mechanisms of extracellular regulation vary greatly depending on context, and many secreted molecules such as Crossveinless-2 (Cv-2) and Sax play diverse roles in different environments (Bangi and Wharton, 2006; Serpe et al., 2008). Thus, whereas *Drosophila* DV patterning does not rely on HSPGs, Sizzled-like molecules, or ADMP, other molecules like Cv-2, Viking, and Sax may play novel mechanistic roles. The feedback mechanisms we selected for the screen are functionally equivalent to those involved in other BMP signaling contexts (Ambrosio et al., 2008; Kelley et al., 2009; Fujise et al., 2003; Wang and Ferguson, 2005; Muraoka et al., 2006). The nine models tested were (1) no feedback, (2) positive feedback of receptor levels, (3) inhibited endocytosis, (4) enhanced endocytosis, (5) inhibited Tld processing, (6) enhanced Tld processing, (7) positive feedback of a surface-bound BMP-binding protein (SBP), (8) decreased release of ligand from ligand-receptor complexes, and (9) enhanced formation of type I-type II-Dpp-Scw complexes (Figure 1C).
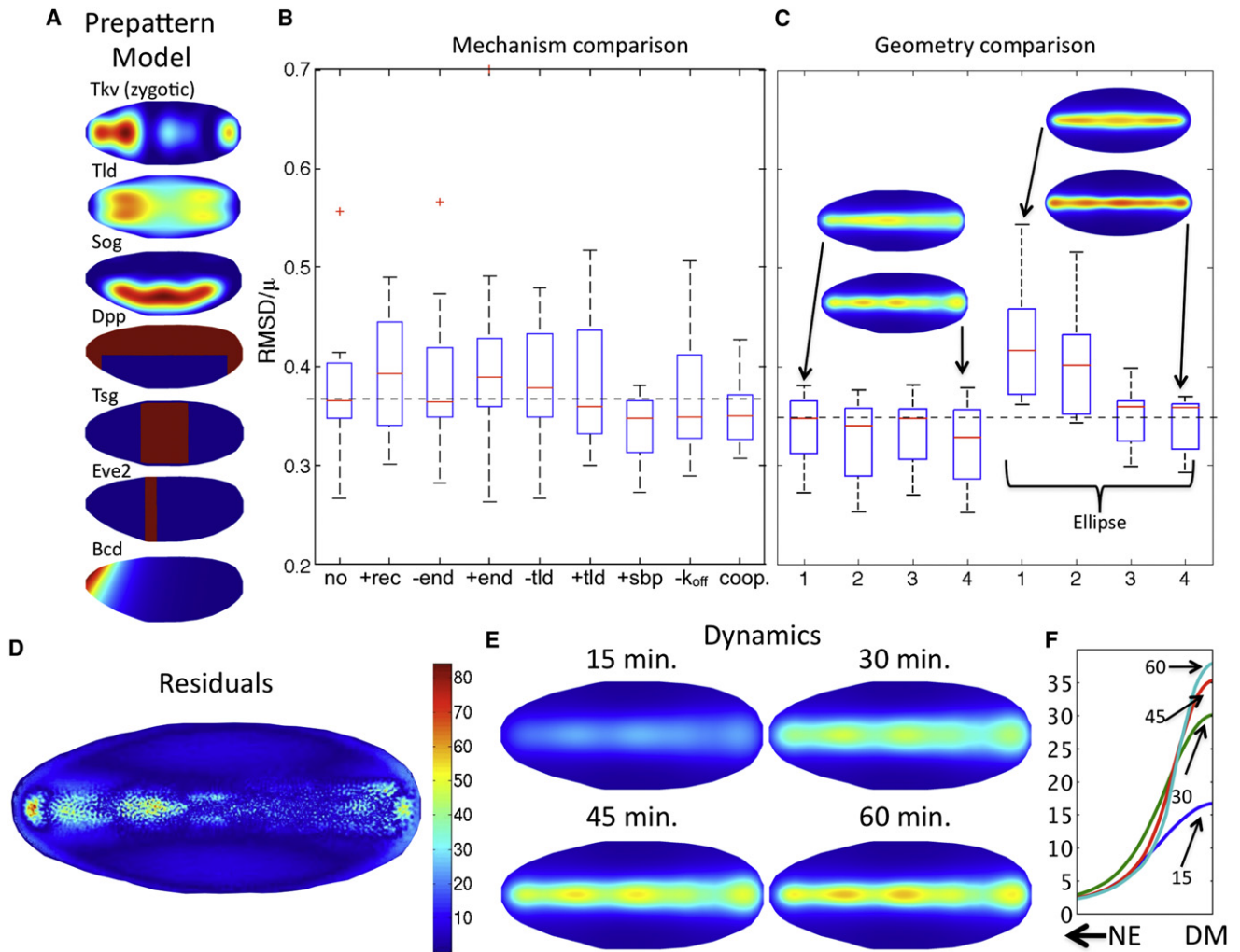
Figure 4. Mechanism Comparison

(A) Prepattern distributions as they appear in the 3D model. The Tld distribution and Sog secretion distribution were determined by fluorescent in situ hybridization of *tld* and *sog* mRNA (method described in [Lecuyer et al., 2007]). The Bicoid distribution was determined by solving a simple reaction-diffusion equation in the periphery of the embryo (Umulis et al., 2008).

(B and C) Box-and-whisker plots of minimum of CV(rmsd) (rmsd/μ) found in the full 3D model for different feedback mechanisms. 50% of all solutions fall within the boxed areas, whereas the whiskers encompass all values within ~2.7 standard deviations of the mean. (B) Contributions of Tkv and Tld nonuniform distributions; (C) embryo shape. The upper and lower limits of the box represent the upper and lower quartile, respectively, and the red line is the median CV(rmsd) value for the series of embryos tested. In (B), the cases compared are: no positive feedback, positive feedback of receptors, negative and positive feedback on endocytosis rates, positive and negative feedback of Tld processing, positive feedback of a BMP-binding nonreceptor, feedback inhibition of ligand release from receptors, and enhanced formation of ligand-type I/II receptor complexes (Wang and Ferguson, 2005; Umulis et al., 2006). In (B), all models were solved with uniform levels of Tkv and Tld. (C) Case 1: uniform Tkv and Tld, Case 2: uniform Tld, nonuniform Tkv, Case 3: uniform Tkv, nonuniform Tld, and Case 4: nonuniform Tld, nonuniform Tkv for the real embryo geometry (first four) and ellipse approximation of embryo geometry.

(D) Typical residual result for the difference between the model result and the mean pMad distribution.

(E) BMP-bound receptor levels begin broad and low and contract in time to produce the nonuniform distribution of occupied receptors.

(F) *BR* levels at $x/L_x = 0.5$.

The "core" reaction-transport equations, which contain no feedback, for dorsal surface patterning are:

$$ligand : \frac{\partial B}{\partial t} = D_B \nabla^2 B + \phi_B(\mathbf{x}) - k_3 I \cdot B + k_{-3} IB + \lambda Tld \cdot IB$$
$$- k_5 B \cdot R + k_{-5} BR, \quad (1)$$

$$Sog : \frac{\partial S}{\partial t} = D_S \nabla^2 S + \phi_S(\mathbf{x}) - k_2 S \cdot T + k_{-2} I, \quad (2)$$

$$Tsg : \frac{\partial T}{\partial t} = D_T \nabla^2 T + \phi_T(\mathbf{x}) - k_2 S \cdot T + k_{-2} I + \lambda Tld \cdot IB - \delta_T T, \quad (3)$$

$$Sog/Tsg : \frac{\partial I}{\partial t} = D_I \nabla^2 I + k_2 S \cdot T - k_{-2} I - k_3 I \cdot B + k_{-3} IB, \quad (4)$$

$$Sog/Tsg/BMP : \frac{\partial IB}{\partial t} = D_{IB} \nabla^2 IB + k_3 I \cdot B - k_{-3} IB - \lambda Tld \cdot IB, \quad (5)$$

$$Receptors: \quad \frac{\partial BR}{dt} = k_5 B \cdot R - k_{-5} BR - \delta_E BR, \qquad (6)$$

$$R_{tot} = R + BR. \qquad (7)$$

Equations 1–7 make up the "no-feedback" model for BMP patterning, and specific equations for each positive-feedback mechanism are provided in Section 3 of the Supplemental Information. Here, **x** is the position in Cartesian coordinates; D_i is the diffusion coefficient for species i; k_j and k_{-j} are the forward and reverse kinetic rate constants, respectively, for reaction j; δ_e is the endocytosis rate; and $\varphi_{ij}(x)$ is the production rate as a function of position for species i. In addition to Equations 1–7, we specify the initial and boundary conditions as determined from image analysis and embryo geometry. The model was solved by using the finite element method.

Each model was trained by optimizing the spatial distribution of BMP-bound receptors (*BR*) predicted by the model against the population mean pMad distribution in *wt* embryos. To measure the best model fit to the experimental data, we calculated the root-mean-square deviation (rmsd) version of the coefficient of variation (CV [rmsd] = rmsd/μ) (Fomekong-Nanfack et al., 2007). The rmsd is a measure of the distance between the normalized model results for the BMP receptor (*BR*) distribution and the corresponding pMad distribution. Here, μ is the average normalized concentration for each image. To remove nonembryo regions from the calculation of CV/rmsd, each image was masked by the x-y orthogonal projection of the mean embryo shape. Typical model results, residuals for the difference between the orthogonal projection of the model against the mean pMad levels, and model dynamics are shown in Figures 4B–4F.

After a base case for each feedback mechanism was determined by optimizing the positive-feedback module against *wt* pMad data, each model was optimized against eight additional mutant data sets by varying a single parameter that corresponds to the respective experimental perturbation. For instance, after a parent parameter set was found for the model that incorporates positive feedback of receptors, the model was then optimized against *bcd > dpp* embryos by changing a single parameter that corresponds to the strength of the *bicoid* driver and expression of the BMP ligand from the anterior end of the embryo. The mutant data sets used for training correspond to the following genotypes: $scw^{+/-}$, $sog^{+/-}$, $tsg^{+/-}$, *bcd > dpp*, *bcd > 2Xdpp*, *bcd > sog*, *bcd > dpp,sog*, and *tsg⁻; bcd > dpp,scw*. To compare alternate feedback mechanisms, we used two measures: (1) comparison of median and upper/lower quartiles for rmsd/μ values (Figure 4B); and (2) comparison of the mean using a t test of significance with α = 0.05. The box plots in Figure 4B suggest that the positive-feedback modules that (1) inhibit endocytosis, (2) increase the Tld processing rate, (3) produce an SBP, (4) slow the release of ligand from receptors, and (5) enhance the formation of ligand-active type I/II receptor complexes have a smaller median CV(rmsd) value than the model with no feedback. However, only the SBP model has a statistically lower mean (p = 0.044) when compared to the model with no feedback. If the significance criterion is relaxed slightly to α = 0.1, receptor cooperativity (p = 0.082) emerges as a good candidate mechanism, whereas the next best feed-

back model has a p value of 0.28. A statistically significant difference means that, on average for a given criterion (e.g., α = 0.05), but not for all the training sets, the model with positive feedback of an SBP produced lower rmsd/μ values when comparing the model and mean population data for each genotype. In some positive-feedback cases (e.g., +rec), the best model fit for a number of the mutant cases was worse than the fit achieved with no feedback, because each mutant case is constrained by the parent set of parameters determined for *wt* embryos.

The SBP positive-feedback model achieves the best overall fit by increasing the binding site density dynamically in response to prior pMad signaling. Here, positive feedback produces a nonsignaling complex that is endocytosed. The increase in binding site density over time dynamically shortens the length scale for BMP transport by increasing the probability of binding to a surface-localized molecule and being endocytosed.

Contributions of Geometry and Prepatterns to Predicted Distributions of BMP-Receptor Complexes

To determine the relative contribution of upstream gene expression and embryo geometry on pMad signaling, we extended the SBP positive-feedback model to include the embryonic prepattern for the relative gene expression of the secreted factors Sog, Tld, and Tkv (Figure 4A) (Fowlkes et al., 2008). For each measured mRNA distribution, we tested a number of different scenarios to calculate the benefit of including expression pattern data as opposed to approximating the distributions by a constant. The expression patterns of *dpp* and *tsg* were approximated from alkaline phosphatase images available in the literature and online (Berkeley *Drosophila* Genome Project) (Mason and Marsh, 1998; Shimmi et al., 2005). To incorporate the imaging data directly into the model, each mean expression pattern is fit to a 2D Fourier sine series and reprojected onto the 3D embryo geometry (Figure 4A; Figure S3). Boundaries from alkaline phosphatase images were approximated by measuring the extents of gene expression for a single embryo.

The sensitivity of the model to the geometrical approximation and upstream gene expression is shown in Figure 4C. For each test, we used the *sog* mRNA distribution as determined by image analysis, and we calculated four different cases for both the real geometry and the ellipsoidal model. Case 1 is uniform Tld and uniform receptors; Case 2 is uniform Tld, nonuniform receptors; Case 3 is nonuniform Tld, uniform receptors; and Case 4 is nonuniform Tld, nonuniform receptors. Surprisingly, the additional biological data did not lead to a substantial reduction in the CV(rmsd) values, but, in the ellipsoidal model, the addition of the nonuniform distributions of Tkv and Tld reduced the CV(rmsd) values by ≈25%. When both nonuniform Tld and Tkv distributions are used in Case 4 of the ellipsoidal model, the CV(rmsd) is nearly equivalent to that in Case 4 in the model with the real embryo geometry. These data suggest that the nonuniform distributions may provide a more reproducible pMad pattern and buffer the system against individual variability in embryo geometry. Additionally, the model not only captures the nonuniform AP distribution of pMad, but also captures the sharpening and contraction of *BR* that correspond well with the observed pMad dynamics (Figures 4E and 4F) (Umulis et al., 2006).

Potential Roles of Type IV Collagen in BMP-Mediated Dorsal Surface Patterning

Although feedback of a "nonreceptor" mechanism is a prediction of the modeling analysis, it has recently been shown that ubiquitous type IV collagen binds Dpp-Scw and may act as an exchange factor that partially regulates ligand-receptor complex formation (Figure 1D) (Wang et al., 2008). Thus, an equivalent positive-feedback mechanism to the SBP model could locally modify the binding affinity between Dpp-Scw and collagen, thereby increasing the binding site density. It has also been suggested that type IV collagen regulates the assembly of the Sog/Dpp-Scw complex, but it is not clear how this impacts the model of BMP patterning (Wang et al., 2008). Type IV collagen is ubiquitously expressed in the blastoderm embryo and binds both Dpp-Scw and Sog. Because the role of secreted binding proteins in the regulation of BMP-receptor interactions has been analyzed elsewhere (Serpe et al., 2008), we focus on mechanisms of collagen-mediated formation of Sog/Dpp-Scw complexes and transport. We developed a modified version of Equations 1–7 to account for the different order of complex formation suggested by Wang et al. (2008). Rather than Sog binding to the cofactor Tsg to form the complex Sog/Tsg, we assumed that Sog and Dpp-Scw bind to collagen, and then bind to each other while attached to collagen. In this scenario, the Sog/Dpp-Scw complex remains bound to the collagen matrix until Tsg binds to Sog/Dpp-Scw to form Sog/Tsg/Dpp-Scw, which is then released from the collagen matrix and thereafter does not rebind. (Equations are given in Supplemental Experimental Procedures.) To keep the model as simple as possible, we made the following assumptions: (1) the binding and release of Dpp-Scw and Sog to collagen is rapid relative to other processes such as production and diffusion and can be treated as having equilibrated (Umulis, 2009); (2) the total amount of collagen does not change in time; and (3) the binding of Sog and Dpp-Scw to collagen is weak. (Biacore binding assays in Wang et al. (2008) support this assumption: for Dpp + Viking, binding $K_D = 746$ nM.) Other balances between the rates of transport to and reaction on an immobile surface are analyzed elsewhere (Othmer, 1976).

To investigate the impact of reduced diffusion rates, we coordinately lowered the diffusion of both Sog and Dpp-Scw and compared the model predictions to the mean distribution of pMad for *wt* embryos. A decrease in the diffusivity of Sog and Dpp-Scw first decreases the rmsd/μ value to a minimum and then increases it again as the effective diffusivity is decreased further (Figure 5A). To investigate whether changing the order of Sog/Tsg/Dpp-Scw complex formation affects the model fit to the data, we measured the rmsd/μ values for two models that differ in the order of ligand-inhibitor complex formation. We observed a moderate increase in the rmsd/μ value in the model in which Sog binds to Dpp-Scw before binding to Tsg, but both models require the rapid formation of the ligand-inhibitor complex (Figure 5B). Earlier 1D models also require the rapid formation of the complex, tight binding, or both and have dissociation constants of 0 nM (irreversible binding) (Eldar et al., 2002), 0.01 nM (binding between Sog/Tsg and ligand) (Mizutani et al., 2005), and 0.03 nM (binding between Sog/Tsg and ligand) (Umulis et al., 2006). Independent of the order of complex formation, when a lower kinetic constant for binding between Sog/Tsg
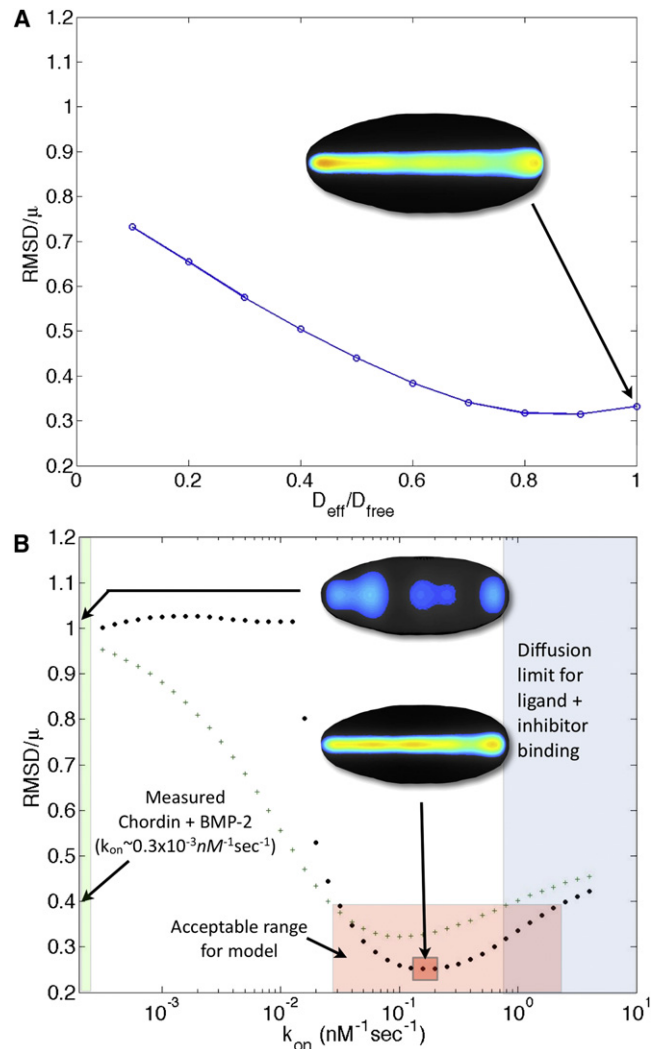

Figure 5. Role for Type IV Collagen in Regulating the Kinetics of BMP-Mediated Patterning of the Dorsal Surface

(A) Decreasing the diffusion coefficients of Sog and Dpp-Scw by 10%–20% decreases the rmsd/μ, but large reductions in the diffusion coefficients lead to progressively higher rmsd/μ values. Inset: model results for the model that includes collagen-mediated formation of Sog/Dpp-Scw complexes. Kinetics are kept constant in (A), and diffusion parameters are kept constant in (B). See the Supplemental Information for parameter values.

(B) rmsd/μ versus the forward binding rate for Dpp-Scw + Sog/Tsg in the original model given by Equations 1–7 ($\cdot$) or Dpp-Scw + Sog in the modified model (+) (Equations 85–91 in the Supplemental Information). The vertical green, shaded region corresponds to the measured dissociation constant for Chordin + BMP-2. The blue, shaded region depicts the diffusion-limited regime for dimerization in solution, and the red, shaded region gives an approximate range for acceptable binding parameters.

and Dpp-Scw (or for binding between Sog and Dpp-Scw) is used in the 3D model, the distribution of *BR* does not agree well with pMad distributions in *wt* embryos (Figure 5B).

The reported kinetics from Biacore analysis for binding between the Sog homolog Chordin (perfused) and the Dpp homolog BMP-2 (immobilized) gives $k_{off} = 3.4 \cdot 10^{-3}$ s, $k_{on} = 0.28 \cdot 10^{-3}$ nM^{-1} s, and a dissociation constant of $K_D = k_{off}/k_{on} \approx 12$ nM (Rentzsch et al., 2006). As shown in

Developmental Cell

Figure 5B, if the measured forward rate of $k_{on} = 0.28 \cdot 10^{-3}\, nM^{-1}\, s^{-1}$ is used in the model, results do not correspond well with observed pMad distributions (Figure 5B).

Many estimates for effective kinetic rates have been developed for ligand-receptor systems by considering the contributions of diffusion-limited transport for molecules to come into contact with each other and the reaction rate of complex formation once the molecules meet (Lauffenburger and Linderman, 1993). There are similar estimates for processes on membranes, where the diffusion coefficients are usually three or more orders of magnitude less (Lauffenburger and Linderman, 1993; Kholodenko et al., 2000). The measured forward rate constant for Chordin binding to BMP-2 ($k_{on} = 0.28 \cdot 10^{-3}\, nM^{-1}\, s^{-1}$) depends on two factors: the diffusion/transport-limited rate constant (k_{diff}) and the intrinsic reaction rate constant (k_r), as shown by Equation 8:

$$\frac{1}{k_{on}} = \frac{1}{k_{diff}} + \frac{1}{k_r}. \qquad (8)$$

The diffusional contribution, k_{diff}, can be approximated by $4\pi Ds$, where D is the sum of the diffusion coefficients of the components ($\approx O[10]\mu s^{-1}$) and $s \approx 5$–10 nm (5 is used) is the encounter radius (Lauffenburger and Linderman, 1993). This leads to the estimate $k_{diff} \approx 0.76\, nM^{-1}\, s$. For BMP-2 + Chordin binding, the measured effective rate constant is $k_{on} = 0.28 \cdot 10^{-3}\, nM^{-1}\, s^{-1}$ (Rentzsch et al., 2006), and using k_{diff} and k_{on} in Equation 8 to solve for k_r gives $k_r \approx k_{on} = 0.28 \cdot 10^{-3}\, nM^{-1}\, s$. This means that, in solution, the binding between Chordin and BMP-2 is reaction limited, and only a small fraction of collisions lead to complex formation. However, as shown in Figure 5B, the model requires forward binding rates that approach the diffusion limit, and not the reaction limit, for binding reactions in solution. If the model requires much tighter and faster binding than the in vitro-determined kinetics for Chordin + BMP-2, how can the model predictions be reconciled with the binding data? Clearly, other factors must be involved, but identifying them is a complex issue that requires a detailed model of all the processes involved, and, to date, this has not been done. Here, we simply suggest how a protein scaffold might influence the formation of multiprotein complexes, and we suggest a scenario in which the rate of formation of Sog/Dpp-Scw may be enhanced by the presence of collagen.

Three basic issues related to transport and reaction kinetics in the presence of collagen can be summarized as follows:

(1) How important are crowding effects in solution, on scaffolds, and on membranes? In particular, how does one correctly describe the transport of molecules along a scaffold or membrane; Is Fick's law appropriate, or does molecular crowding and volume exclusion (Grasberger et al., 1986) require a more detailed constitutive relation? A recent prediction concerning crowding is that, for a fixed number of reacting particles, there is an optimal density of obstacles in solution that minimizes the time needed for a random walker to find a target (Schmidt et al., 2009). If the density is too low, the particles cannot find each other, whereas if it is too high, diffusion limits impede the rate of formation.

(2) If localized collagen leads to local increases in the concentration of both Sog and Dpp-Scw, can this lead to a sufficient increase in the rate of complex formation on collagen?

(3) How do the free-energy changes of bimolecular interactions change on a surface, as compared with solution? Can one predict with sufficient accuracy the relationship between the kinetic constants for reactions on the surface knowing kinetic constants measured in well-mixed solutions? This involves steric factors, such as better alignment on the surface, that will usually change from solution to surface, as well as differences in the internal energy of the molecules in the two environments.

While crowding effects, free-energy changes, and local increases in concentration can affect dimerization and complex formation once attached to collagen, little data are available regarding the first and third factors, and we focus solely on the second: how collagen may increase the formation rates by concentrating Sog and Dpp-Scw.

Once bound to collagen, the diffusion of Sog and Dpp-Scw molecules would be greatly reduced, and the rate of the formation of Sog/Dpp-Scw complexes may well be transport limited. To determine how collagen modifies the rate of the formation of complexes, we investigated two possibilities: (1) collagen is tightly localized to the inner membrane of the PV space, and (2) collagen extends a distance, h, into the PV space, which has overall height L_z (Section 4 of the Supplemental Information). If collagen is localized tightly near the surface of the cells that line the PV space, we can approximate the collagen matrix as a thin sheet (2D) and use the diffusion limit $k^{2D} \approx 2\pi D/\ln(b/s)$, where b is one-half the mean distance between molecule on the surface, D is the diffusion coefficient for molecules attached to collagen on the surface, and s is the encounter radius (Lauffenburger and Linderman, 1993). (For the derivation of the equations relating to collagen-mediated complex formation, see Section 4 of the Supplemental Information.) A typical value for the diffusion-limited binding reactions in 2D is $k+ \approx 3 * 10^{-1}\, \mu^2\, s^{-1}$ (Lauffenburger and Linderman, 1993).

In the absence of Tsg, the change in the number of Sog/Dpp-Scw complexes (N_{SBtot}) in time is the sum of the rates of binding and release of Sog (S) + Dpp-Scw (B) in solution and the rates of binding and release of collagen-bound Sog (SC_n) and bound Dpp-Scw (BC_n), where C_n is collagen. For simplicity, we only discuss the result for a 2D collagen matrix layer of area A at the base of the PV space (volume = AL_z), and we assume that the concentration is spatially uniform; the governing equation is:

$$\frac{\partial N_{SBtot}}{\partial t} = \underbrace{A \cdot L_z (k_{on} B \cdot S - k_{off} \overline{SB})}_{\text{formation solution}} \underbrace{A (k_+ \overline{BC_n} \cdot \overline{SC_n} - k_- \overline{BC_n SC_n})}_{\text{formation collagen}}. \qquad (9)$$

The areal concentrations (with units of [mol./area]) of collagen-bound BMP (BC_n) and collagen-bound Sog (SC_n) depend on the total density, C_{nT}, of collagen present and the binding kinetics between Collagen + Sog and Collagen + Dpp-Scw. If the dissociation constant for Collagen + Sog is K_S and for Collagen + Dpp-Scw is K_B, and the surface binding reactions are fast relative to

other processes, we can determine an effective formation rate for the 2D reactions. Dividing Equation 9 by the volume (L_zA), defining $\mathbf{C_{nT}} = C_{nT}/L_z$ and $\mathbf{BC_nSC_n} = BC_nSC_n/L_z$ as the volumetric concentrations by averaging the surface densities over the local volume, and simplifying gives:

$$\frac{\partial \overline{SB}_{tot}}{\partial t} = k_{on}B \cdot S - k_{off}\overline{SB} + (k_+ L_z)\Omega\, B \cdot S - k_- \overline{\mathbf{BC_nSC_n}}. \quad (10)$$

Here, $k_+ L_z$ is a second-order rate constant for the surface reaction, with units ($[\text{mol.}/\text{L}^3\text{time}]^{-1}$), and the ratio $\Omega \equiv \mathbf{C_{nT}^2}/(K_BK_S)$ is dimensionless. For a relatively slow 2D diffusion-limited surface reaction, $k_+ \approx 3 \times 10^{-1}\mu^2\,\text{s}^{-1}$ (Lauffenburger and Linderman, 1993). If the collagen binding site density is of order $30/\mu^2$, if K_B and K_S are of order 100 nM, and L_z is taken as the height of the PV space (0.5 μm), then Ω is on the order of 1, and this leads to the estimate $k_+ L_z \approx 0.1\,\text{nM}^{-1}\,\text{s}^{-1}$. The collagen-mediated rate of $k_+ L_z \approx 0.1\,\text{nM}^{-1}\,\text{s}^{-1}$ is in the range needed for proper pattern formation in the model (Figure 5B). This rate is $\approx 320\times$ greater than the binding between free Sog and Dpp-Scw in solution, but of course it is predicated on the estimates used. If both binding constants are 1 μM (recall K_B for Dpp + Viking is ≈ 746 nM), the estimated rate is only 3.2 times that in solution. The density of binding sites may be much higher as well, and Ω could still be in the range necessary to provide a substantial boost in the kinetics of Dpp-Scw + Sog complex formation. If $k_- \approx k_{off}$ and $(k_+ L_z\Omega)/k_{on} \gg 1$, then the effective dissociation constant for the total concentration of complexes (SB_{tot}) is $K_D \approx k_{off}/(k_+ L_z\Omega) \approx 0.03$ nM, which is exactly in the range necessary for peak formation by the shuttling mechanism with freely diffusible Sog and Dpp-Scw. Similar relationships can also be derived by assuming two different volume fractions in the PV space; however, in those cases as well, the conclusions are contingent on estimates of unknown rates. If the above-described estimates hold, the increase in the apparent kinetic rate constant in going from solution to the collagen matrix can be very large and far exceeds the potential reduction in kinetic constants by slowing the diffusion of binding partners once attached to collagen.

However, one problem remains: the Sog/Dpp-Scw complex is still attached to the collagen matrix, which would hinder transport and potentially the reaction with other regulators. A possible resolution of this problem was also presented recently in the context of *Drosophila* (Wang et al., 2008). Specifically, the results indicate that the cofactor Tsg facilitates the release of the Sog/Dpp-Scw complex from the type IV collagen during *Drosophila* embryonic patterning (Wang et al., 2008). After release, the Sog/Tsg/Dpp-Scw complex could then participate in other processes such as Tld-mediated cleavage of Sog, which would release the Dpp-Scw ligand for signaling. If Tsg facilitates the release relatively rapidly, the results presented in Wang et al. (2008) imply an interesting caveat that should be considered when thinking about mechanisms of BMP regulation. The effective amount of Sog/Dpp-Scw in solution (the mobile phase) is controlled by processes on the surface that occur very rapidly and favor the formation of the complex. The limiting step for the formation of the complex would be binding to the type IV collagen or other binding site (perhaps Cv-2).

Model Results for Ectopic Gene Expression of BMP Regulators

With the full 3D model, we can calculate the *BR* distributions for various Gal4-UAS experiments, determine the relative strength of the driver-responder combinations, and make predictions to further elucidate BMP regulation. We calculated the *BR* distribution for over 15 Bicoid-Gal4-UAS experiments for which pMad distributions were available, and although the model captures many aspects of the experimental images, it does not produce qualitatively similar results for every combination (Figures 6A–6V and 6A′–6V′).

In particular, the model captures the expected distributions in a number of ectopic gene expression experiments, including the rescue of *tsg-;bcd > tsg*, the residual pMad signaling in *bcd > tld,dpp,sog* and *bcd > sog,dpp* embryos. Intriguingly, the model results do not correspond well with the pMad distributions in Figures 6D, 6E, and 6R. In each of these cases, the predicted *BR* levels at the anterior end are higher than the observed pMad distribution. All three examples correspond with increased expression of BMP ligands near the anterior end of the embryo. It is remarkable that pMad signaling is so low in a region in which there should be a large amount of BMP ligands. In Figure 6R, the model predicts high levels of *BR* near the dorsal midline, whereas the pMad distribution "splits" into two lateral stripes. (Additional modeling results are given in Figure S5.) The signaling gaps observed in Figures 6B, 6D, 6E, and 6R are reminiscent of the pMad signaling gaps observed in embryos with ectopic addition of activated *tkv*[act] mRNA (Wang and Ferguson, 2005) (Figures 6S and 6S′). To determine if the model could capture the signaling gap observed in the *tkv*[act] mRNA experiments, we simulated the ectopic addition of a fixed amount of mRNA at the anterior end and measured two quantities: the expected level of pMad signaling, which is the sum of Tkv[act] and *BR*, and the total distribution of surface-associated BMP. Remarkably, the model captures the observed features in both the expected pMad distribution and the level of surface-localized BMP (Figures 6S and 6S′), including the signaling shadow between the Tkv[act] pool in the posterior and *BR* in the anterior (Figure 6S) and the anterior-facing wavefront of surface-localized BMP (Figure 6S′) (Figure S5). According to the model, the additional binding of Dpp-Scw to receptors provides a sink that dynamically lowers the range of Dpp-Scw. The limited distribution of Dpp-Scw affects the distribution of Sog/Tsg/Dpp-Scw complexes, which ultimately changes the directionality of the Dpp-Scw flux. The shadows result from the dynamic imbalance of Dpp-Scw binding and Sog/Tsg-mediated transport.

Scale Invariance of BMP-Mediated Signaling

The data presented above clearly indicate that the specific embryo geometry has a large impact on the ability of the model to predict levels of *BR* that are in quantitative agreement with the observed pMad distributions. Geometry predominately impacts the distances traveled by BMPs, and thus the range of ligands and inhibitors will vary along the AP axis. One would expect that a patterning process dependent on domain geometry would also depend on the overall size or scale of the domain. In general, reaction-diffusion equations similar to those used for BMP patterning are highly dependent on the length-scale of the system and do not lead to the preservation of
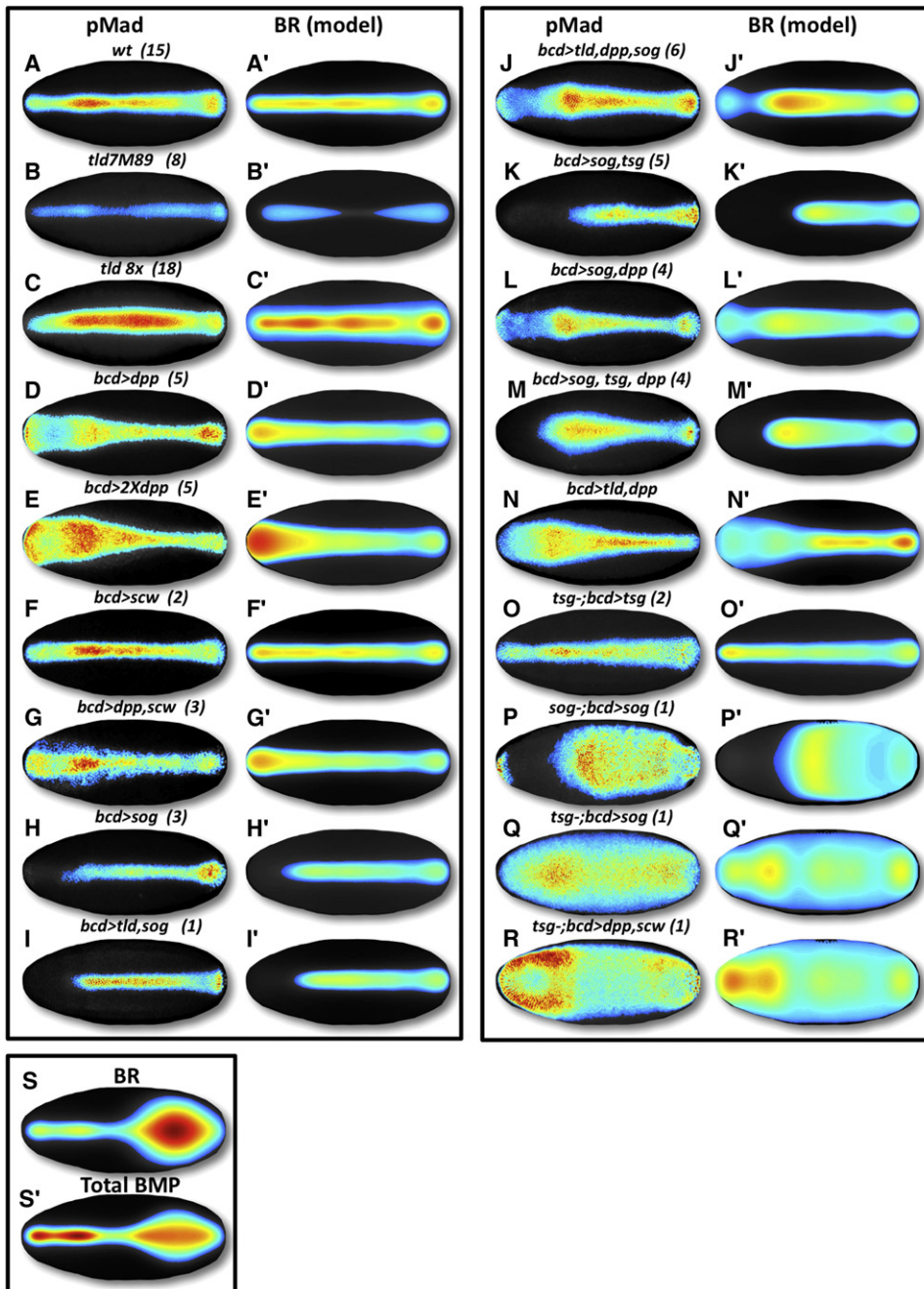
Developmental Cell

Figure 6. 3D Model Results

(A–S′) (A–S) Mean pMad staining for ectopic gene expression experiments and/or mutant alleles. (A′–S′) Levels of *BR* calculated by using the computational model. See Section 3 of the Supplemental Information and Figure S8 for additional discussion of the *tld*[7M89] allele.

proportion observed in numerous biological contexts (Othmer and Pate, 1980).

A recent theoretical study of BMP patterning of *Xenopus laevis* embryos suggests that a single-ligand shuttling mechanism does not lead to scale invariance. In *Xenopus*, scale invariance might actually be mediated by the combined action of two types of ligands: the BMPs and ADMP. However, ADMP is absent in *Drosophila*, which suggests one of two possibilities: (1) BMP

signaling between different sized embryos is not scale invariant; or (2) alternative mechanisms to the proposed mechanism for *Xenopus* BMP scaling lead to *Drosophila* BMP patterning scale invariance. To investigate the question of scaling, we calculated the distribution of *BR* in the 3D model by increasing the size of the embryo while keeping all other quantities constant. The "shuttling-only" mechanism with fixed production rates (concentration/time) and fixed receptor concentrations
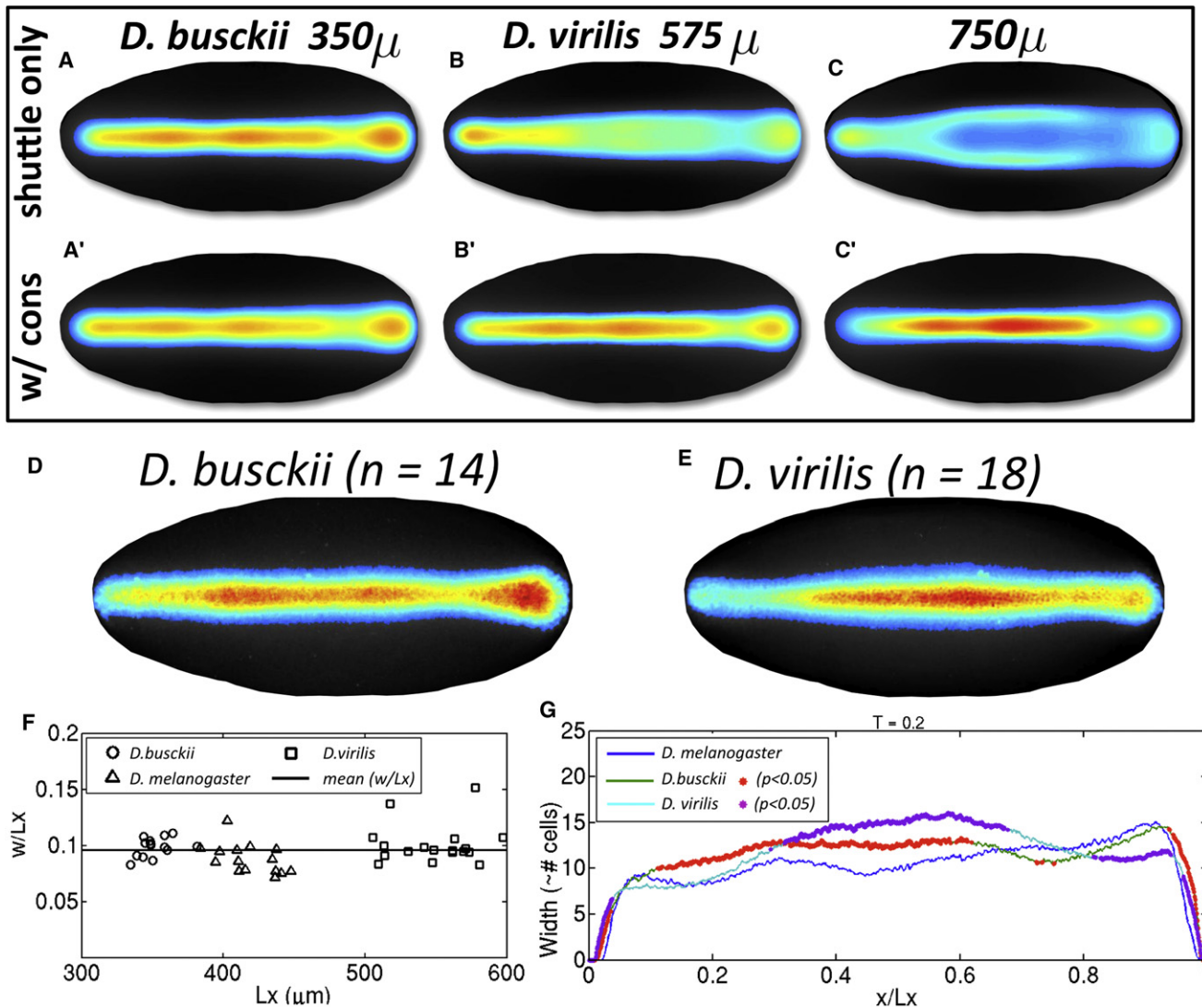
Figure 7. Mechanisms of Morphogen Scale Invarience-Calculated *BR* Levels for *D. virilis* and *D. busckii* and Predicted Distribution for Embryos 750 μm in Length

(A–C′) (A–C) The expected *BR* levels when conservation conditions are imposed for the total amounts of protein production, and/or protein levels, are shown. (A′–C′) Same as (A)–(C), except without conservation on the total amount of production/proteins in the system (i.e., the concentrations are constant).

(D and E) Distribution of pMad signaling in (D) *D. busckii* (n = 14) and (E) *D. virilis* (n = 18).

(F) Average pMad width along the AP axis is constant between species.

(G) Scale invariance does not occur at all positions along the AP axis because the shape of the pMad distribution is different between species.

does not lead to scale invariance of the *BR* distribution. Whereas the *BR* distribution is largely unchanged in smaller embryos (Figure 7A) that correspond roughly with the size expected for *D. busckii* (Gregor et al., 2005), the pattern of *BR* in embryos ≈575 μm in length (Figure 7B) is qualitatively different than the pattern predicted in *D. melanogaster* (≈400 μm in length). In simulations in which the embryo is slightly larger than expected for *D. virilis* or ≈750 μm in length, the pattern of *BR* splits at ≈25% embryo length and leads to two parallel stripes that reconverge at the posterior pole (Figure 7). Before measuring pMad signaling in different size embryos, we tested how an alternative scale-invariance hypothesis might impact the model-predicted results.

Neglecting positive feedback for a moment, Equations 1–7 show that the distribution of *BR* complexes depends on a number of linear and nonlinear reactions that occur in the perivitelline space. Specifically, the level of *BR* depends on the level of free BMP ligands, which, in turn, depends on four kinetic processes: (1) production of ligand, (2) binding and release to the Sog/Tsg complex, (3) receptor binding and release, and (4) release from the inhibitor complex by the destruction of Sog by Tld. If we first consider Equations 1–7 with zero production of Sog, the equation for Tsg becomes decoupled from the equations for BMP ligands and receptors. In the zero Sog scenario, the level of *BR* depends only on interactions between ligand and receptors. This leads to the simplified set of equations for

Developmental Cell

BMP-receptor dynamics (Equations 11 and 12) that are similar to those proposed for dynamic scale invariance of AP patterning of *Drosophila* embryos by Bcd (Umulis, 2009; Gregor et al., 2007a; Umulis et al., 2008):

$$BMP - ligand : \frac{\partial B}{\partial t} = D_B \nabla^2 B + \phi_B(\mathbf{x}) - k_5 B \cdot R_{tot} + (k_5 B + k_{-5})BR, \tag{11}$$

$$Receptors : \frac{\partial BR}{dt} = k_5 B \cdot R_{tot} - (k_5 B + k_{-5} + \delta_E)BR. \tag{12}$$

Replacing the ∇^2 by $L^{-2}\overline{\nabla}^2$, assuming binding equilibration in the linear range, and adding Equations 11 and 12 make the requirements for scale invariance of the simplified system more transparent:

$$BMP - ligand : \frac{\partial B}{\partial t} = \frac{D_B/L^2}{1 + R_{tot}/K_m}\overline{\nabla}^2 B + \frac{\phi_B^*(\underline{\xi})}{1 + R_{tot}/K_m}$$
$$- \delta_E \frac{R_{tot}/K_m}{1 + R_{tot}/K_m}B, \tag{13}$$

$$\underline{\xi} = \mathbf{x}/L. \tag{14}$$

Previously, we have suggested, for linear morphogen patterning systems, that scale invariance occurs automatically if the following conditions are met (Umulis, 2009; Umulis et al., 2008):

- Patterning occurs along a surface. (Dimensional analysis suggests that the PV space can be approximated as a 2D surface wrapped around a 3D core.)
- Proportions are constant between individuals that differ in size, which means that, for a constant PV space thickness, the area (A) scales in proportion to the characteristic length squared (i.e., $A \propto \sigma L^2$). This is true within a species, and approximately true between different species.
- The total number of binding sites, decay rates, and other processes that may naturally scale with size are constant. This is true, for instance, if receptor levels in the PV space scale with nuclear density.
- Constant total morphogen production in molecules/time (Hypothesis).
- Morphogen gradient interpretation by total binding site occupancy (molecules) and not the total concentration (molecules/area) of occupied binding sites. (Hypothesis. This has been demonstrated for receptor occupancy and Activin signaling, but this has not yet been tested for BMPs in *Drosophila* [Dyson and Gurdon, 1998].)

Constancy of total receptor number and total production rates (molecules/time) leads to $R_{tot} = N_{tot}/(\sigma L^2)$ and $\phi_B^*(\underline{\xi}) = \Phi_B(\underline{\xi})/L^2$. Imposing these conditions on Equation 13, and defining $\Lambda = N_{tot}/(\sigma K_m)$ leads to Equation 15:

$$\frac{\partial B}{\partial t} = \underbrace{\frac{1}{\underbrace{\Lambda + L^2}_{f(L)}}}_{} \underbrace{\left[D_B\overline{\nabla}^2 B + \Phi_B(\xi) - \delta_E \Lambda B\right]}_{L-independent}. \tag{15}$$

In the "zero Sog" case given by Equation 15, the level of free BMP ligand is automatically scale invariant at steady state and

may also be scale invariant dynamically during the approach to steady-state depending on the value of Λ. With Sog secretion, the situation is much more complicated, primarily due to the nonlinear binding steps that occur between Sog, Dpp-Scw, and Tsg in the PV space. However, the conservation may lead to some scale invariance, even if it is not "perfect" scale invariance, as can be shown for linear systems. To test the scale invariance of the full patterning model, we hypothesized that the secretion of zygotic Dpp-Scw, Sog, Tsg, and the total level of Tld, receptors, and feedback rates in the PV space scale with the number of nuclei as outlined above. The model results deviate less from the *D. melanogaster* predictions, but the patterns are not perfectly scale invariant (Figures 7A′–7C′). The shape of the *BR* distribution changes in different-sized embryos, but the difference between predicted patterns in embryos becomes much more pronounced, as the size is increased from the 400 μm length used for the *D. melanogaster wt* base case. The difference in the patterns between the shuttling-only model and the model that includes constancy of secretion rates is also much more pronounced as the simulated embryo size becomes larger (compare Figures 7B, B′, 7C, and 7C′). Because there are large qualitative differences between the predictions made by the two mechanisms, and it was not clear a priori that dorsal surface patterning is actually scale invariant, we stained for pMad signaling in *D. busckii* (≈350 μm) and *D. virilis* (≈575 + μm) (Figures 7D–7G). We found that the ratio of mean width to embryo length (w/L_x) for pMad (T = 0.2) along the AP axis is scale invariant, but it is not an example of a "perfectly" scale-invariant system. Instead, whereas w/L_x is constant between species, the shape of the distribution deviates from *D. melanogaster* at different positions along the AP axis. Intriguingly, pMad staining in *D. virilis* is more consistent with a mechanism employing conservation conditions than without the conditions (Figures 7B, 7B′, and 7E). In the model predictions for embryos 575 μm and 750 μm in length, *BR* levels begin to diminish at the poles, the profile bows out near the AP midline, and the maximum amplitude shifts from the position at approximately one-third the embryo length to approximately one-half the embryo length. This is consistent with the mean pMad observed in *D. virilis* and is also consistent with our preliminary data for pMad staining in *Musca domestica* embryos.

The Relationship between Embryo Geometry and Dorsal Surface Patterning

Lastly, we were interested in how changes in embryo proportion impact the model-predicted distributions of *BR*. To test this, we scaled the model geometry for the embryo along the x axis only, keeping the y and z scales constant. Furthermore, we tested both the shuttling-only and shuttling with conservation condition models and show the results of the latter here (Figure 8). For the simulations, we assumed that the mRNA prepatterns were scaled consistently with the geometric scalings. The predicted patterns change appreciably as the geometry of the embryo is changed. In "short" embryos, *BR* levels bow out and accumulate at the poles where Sog would be lowest and Tld highest. In 0.75× embryos, *BR* forms three local maxima at ≈25%, 33%, and 75% embryo length, and as embryos are stretched in the x direction beyond 1.0×, pMad signaling is lost at ≈25% and 75% embryo length.
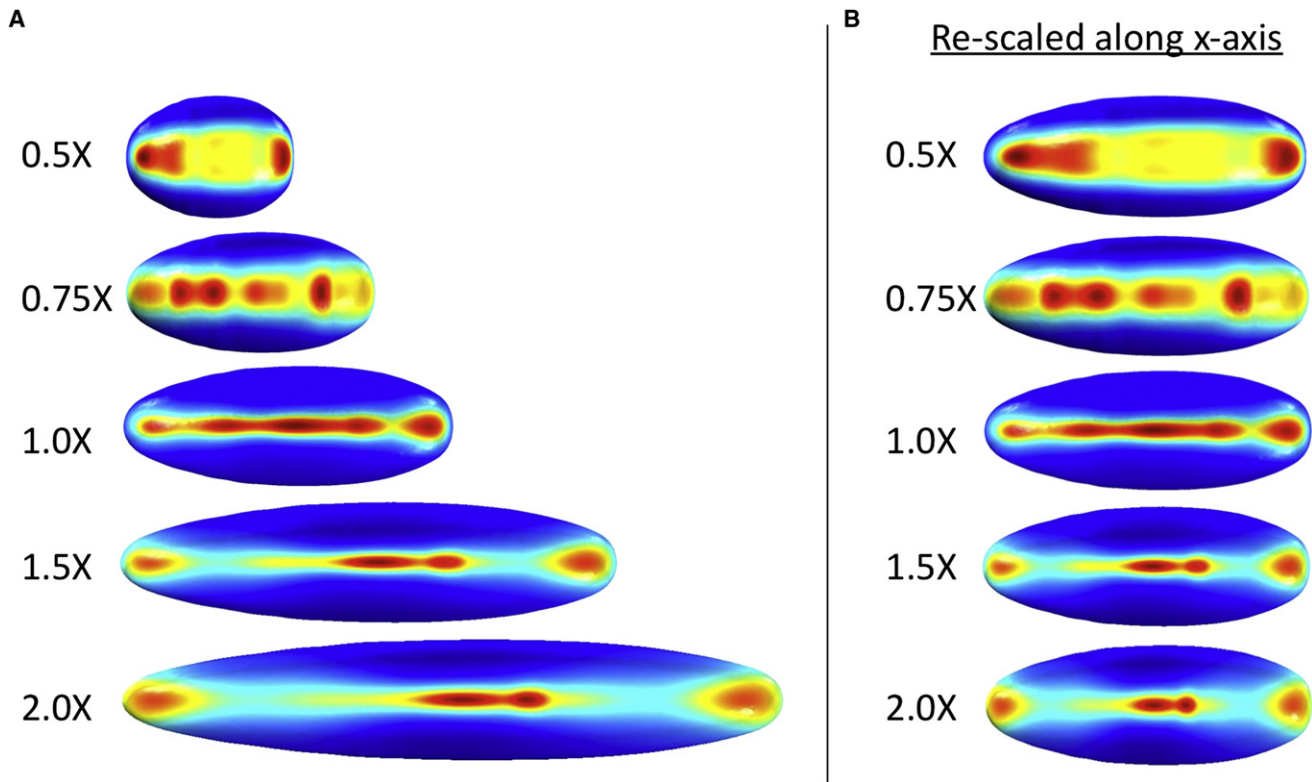
Figure 8. Predicted Relationship between Model-Predicted Distribution of *BR* and Different Embryo Shapes

(A and B) For each simulation, the mRNA prepattern information was scaled in proportion to the embryo shape changes.

Future Directions

The model results for mechanisms of scale invariance, collagen, and the relationship between shape and pattern can be experimentally tested to support or refute the ''predictions'' made in this paper. First, to test the relationship between nuclear density, binding site density (i.e., Tkv and Collagen), and pMad patterning, one could stain for pMad signaling in embryos in which the local density of nuclei is disrupted, as was done to demonstrate the relationship between nuclei and dpERK patterning (Coppey et al., 2008). To investigate the dependence of dorsal surface patterning on shape, one could quantitatively measure pMad signaling in other species of *Drosophila* such as *D*. *pseudoobscura*, *D*. *erecta*, or other *Diptera*, including *Lucilla sericata*, which have embryo shapes that differ significantly from *D*. *melanogaster* (Gregor et al., 2005; Lott et al., 2007).

There are a number of ways to extend the current model to address new and emerging questions of pattern formation. First, one could couple the computational modeling framework with the SpatioTemporal atlases of gene expression to test alternative mechanisms of AP patterning and crosstalk between the AP and DV signals (Fowlkes et al., 2008). Numerous genes are not strictly AP or DV spanning, and their expression is the result of dynamically integrating signals that originate along orthogonal axes. 3D spatiotemporal modeling of *Drosophila* provides a robust platform on which to investigate the mechanisms of signal integration.

Another extension of this work is to develop a coupled volumetric/surface patterning embryonic model to understand the balance of processes for Bicoid transport along the AP axis (Bergmann et al., 2007; Gregor et al., 2007a; Umulis et al., 2008; Spirov et al., 2009). Earlier, we simulated the Bicoid transport problem at the embryo periphery for the ectopic expression simulations, but during the last four nuclear division cycles, there is exchange of Bicoid between nuclei that line the periphery and the embryo core that conspires to produce a quasi-steady state of nuclear Bicoid concentration (Gregor et al., 2007a; Coppey et al., 2007). Furthermore, with the full 3D model, we are not limited to transport by diffusion, and one could extend AP patterning studies to include cytoplasmic movement and directed transport (Gregor et al., 2007a; Foe and Alberts, 1983; Hecht et al., 2009).

Developmental Cell

REFERENCES

Ambrosio, A.L., Taelman, V.F., Lee, H.X., Metzinger, C.A., Coffinier, C., and De Robertis, E.M. (2008). Crossveinless-2 is a BMP feedback inhibitor that binds Chordin/BMP to regulate Xenopus embryonic patterning. Dev. Cell *15*, 248–260.

Bangi, E., and Wharton, K. (2006). Dual function of the *Drosophila* Alk1/Alk2 ortholog Saxophone shapes the Bmp activity gradient in the wing imaginal disc. Development *133*, 3295–3303.

Bergmann, S., Sandler, O., Sberro, H., Shnider, S., Schejter, E., Shilo, B.Z., and Barkai, N. (2007). Pre-steady-state decoding of the Bicoid morphogen gradient. PLoS Biol. *5*, e46.

Coppey, M., Berezhkovskii, A., Kim, Y., Boettiger, A., and Shvartsman, S. (2007). Modeling the bicoid gradient: diffusion and reversible nuclear trapping of a stable protein. Dev. Biol. *312*, 623–630.

Coppey, M., Boettiger, A., Berezhkovskii, A., and Shvartsman, S. (2008). Nuclear trapping shapes the terminal gradient in the *Drosophila* embryo. Curr. Biol. *18*, 915–919.

Driever, W., and Nusslein-Volhard, C. (1988). The bicoid protein determines position in the *Drosophila* embryo in a concentration-dependent manner. Cell *54*, 95–104.

Dyson, S., and Gurdon, J.B. (1998). The interpretation of position in a morphogen gradient as revealed by occupancy of activin receptors. Cell *93*, 557–568.

Eldar, A., Dorfman, R., Weiss, D., Ashe, H., Shilo, B.Z., and Barkai, N. (2002). Robustness of the BMP morphogen gradient in *Drosophila* embryonic patterning. Nature *419*, 304–308.

Foe, V.E., and Alberts, B.M. (1983). Studies of nuclear and cytoplasmic behaviour during the five mitotic cycles that precede gastrulation in *Drosophila* embryogenesis. J. Cell Sci. *61*, 31–70.

Fomekong-Nanfack, Y., Kaandorp, J., and Blom, J. (2007). Efficient parameter estimation for spatio-temporal models of pattern formation: case study of *Drosophila melanogaster*. Bioinformatics *23*, 3356–3363.

Fowlkes, C.C., Hendriks, C.L., Kernen, S.V., Weber, G.H., Rübel, O., Huang, M.Y., Chatoor, S., DePace, A.H., Simirenko, L., Henriquez, C., et al. (2008). A quantitative spatiotemporal atlas of gene expression in the *Drosophila* blastoderm. Cell *133*, 364–374.

Fujise, M., Takeo, S., Kamimura, K., Matsuo, T., Aigaki, T., Izumi, S., and Nakato, H. (2003). Dally regulates dpp morphogen gradient formation in the *Drosophila* wing. Development *130*, 1515–1522.

Grasberger, B., Minton, A.P., DeLisi, C., and Metzger, H. (1986). Interaction between proteins localized in membranes. Proc. Natl. Acad. Sci. USA *83*, 6258–6262.

Gregor, T., Bialek, W., de Ruyter van Steveninck, R.R., Tank, D.W., and Wieschaus, E.F. (2005). Diffusion and scaling during early embryonic pattern formation. Proc. Natl. Acad. Sci. USA *102*, 18403–18407.

Gregor, T., Wieschaus, E.F., McGregor, A.P., Bialek, W., and Tank, D.W. (2007a). Stability and nuclear dynamics of the bicoid morphogen gradient. Cell *130*, 141–152.

Gregor, T., Tank, D.W., Wieschaus, E.F., and Bialek, W. (2007b). Probing the limits to positional information. Cell *130*, 153–164.

Hecht, I., Rappel, W.J., and Levine, H. (2009). Determining the scale of the Bicoid morphogen gradient. Proc. Natl. Acad. Sci. USA *106*, 1710–1715.

Kelley, R., Ren, R., Pi, X., Wu, Y., Moreno, I., Willis, M., Moser, M., Ross, M., Podkowa, M., Attisano, L., and Patterson, C. (2009). A concentration-dependent endocytic trap and sink mechanism converts Bmper from an activator to an inhibitor of Bmp signaling. J. Cell Biol. *184*, 597–609.

Kholodenko, B.N., Hoek, J.B., and Westerhoff, H.V. (2000). Why cytoplasmic signalling proteins should be recruited to cell membranes. Trends Cell Biol. *10*, 173–178.

Lauffenburger, D., and Linderman, J. (1993). Receptors: Models for Binding, Trafficking, and Signaling (New York: Oxford University Press).

Lecuyer, E., Yoshida, H., Parthasarathy, N., Alm, C., Babak, T., Cerovina, T., Hughes, T., Tomancak, P., and Krause, H. (2007). Global analysis of mRNA localization reveals a prominent role in organizing cellular architecture and function. Cell *131*, 174–187.

Lott, S.E., Kreitman, M., Palsson, A., Alekseeva, E., and Ludwig, M.Z. (2007). Canalization of segmentation and it evolution in *Drosophila*. Proc. Natl. Acad. Sci. USA *104*, 10926–10931.

Mason, E.D., and Marsh, J.L. (1998). Changes in the pattern of twisted gastrulation gene expression among *Drosophila* species. J. Mol. Evol. *46*, 180–187.

Mizutani, C.M., Nie, Q., Wan, F.Y., Zhang, Y.T., Vilmos, P., Sousa-Neves, R., Bier, E., Marsh, J.L., and Lander, A.D. (2005). Formation of the BMP activity gradient in the *Drosophila* embryo. Dev. Cell *8*, 915–924.

Muraoka, O., Shimizu, T., Yabe, T., Nojima, H., Bae, Y.K., Hashimoto, H., and Hibi, M. (2006). Sizzled controls dorso-ventral polarity by repressing cleavage of the Chordin protein. Nat. Cell Biol. *8*, 329–338.

O'Connor, M.B., Umulis, D.M., Othmer, H.G., and Blair, S.S. (2006). Shaping BMP morphogen gradients in the *Drosophila* embryo and pupal wing. Development *133*, 183–193.

Othmer, H.G. (1976). Nonlinear wave propagation on reacting systems. J. Math. Biol. *2*, 133–163.

Othmer, H.G., and Pate, E. (1980). Scale-invariance in reaction-diffusion models of spatial pattern formation. Proc. Natl. Acad. Sci. USA *77*, 4180–4184.

Reeves, G.T., Muratov, C.B., Schpbach, T., and Shvartsman, S.Y. (2006). Quantitative models of developmental pattern formation. Dev. Cell *11*, 289–300.

Rentzsch, F., Zhang, J., Kramer, C., Sebald, W., and Hammerschmidt, M. (2006). Crossveinless 2 is an essential positive feedback regulator of Bmp signaling during zebrafish gastrulation. Development *133*, 801–811.

Schmidt, J.D., Kamber, E., and Kondev, J. (2009). Lattice model of diffusion-limited bimolecular chemical reactions in confined environments. Phys. Rev. Lett. *102*, 218302.

Schmierer, B., Tournier, A.L., Bates, P.A., and Hill, C.S. (2008). Mathematical modeling identifies Smad nucleocytoplasmic shuttling as a dynamic signal-interpreting system. Proc. Natl. Acad. Sci. USA *105*, 6608–6613.

Serpe, M., Umulis, D., Ralston, A., Chen, J., Olson, D., Avanesov, A., Othmer, H., O'Connor, M., and Blair, S. (2008). The BMP-binding protein Crossveinless 2 is a short-range, concentration-dependent, biphasic modulator of BMP signaling in *Drosophila*. Dev. Cell *14*, 940–953.

Shimmi, O., Umulis, D., Othmer, H., and O'Connor, M. (2005). Facilitated transport of a Dpp/Scw heterodimer by Sog/Tsg leads to robust patterning of the *Drosophila* blastoderm embryo. Cell *120*, 873–886.

Spirov, A., Fahmy, K., Schneider, M., Frei, E., Noll, M., and Baumgartner, S. (2009). Formation of the bicoid morphogen gradient: an mRNA gradient dictates the protein gradient. Development *136*, 605–614.

Sutherland, D.J., Li, M., Liu, X.-Q., Stefancsik, R., and Raftery, L.A. (2003). Stepwise formation of a SMAD activity gradient during dorsal-ventral patterning of the *Drosophila* embryo. Development *130*, 5705–5716.

Turing, A. (1952). The chemical basis of morphogenesis. Phil. Trans. R. Soc. Lond. *237*, 37–72.

Umulis, D.M. (2009). Analysis of dynamic morphogen scale-invariance. J. R. Soc. Interface *6*, 1179–1191.

Umulis, D.M., Serpe, M., O'Connor, M.B., and Othmer, H.G. (2006). Robust, bistable patterning of the dorsal surface of the *Drosophila* embryo. Proc. Natl. Acad. Sci. USA *103*, 11613–11618.

Umulis, D.M., O'Connor, M.B., and Othmer, H.G. (2008). Robustness of embryonic spatial patterning in *Drosophila melanogaster*. Curr. Top. Dev. Biol. *81*, 65–111.

Wang, X., Harris, R., Bayston, L., and Ashe, H. (2008). Type IV collagens regulate BMP signalling in *Drosophila*. Nature *455*, 72–77.

Wang, Y.C., and Ferguson, E.L. (2005). Spatial bistability of Dpp-receptor interactions during *Drosophila* dorsal-ventral patterning. Nature *434*, 229–234.

Wolpert, L. (1969). Positional information and the spatial pattern of cellular differentiation. J. Theor. Biol. *25*, 1–47.